AIRCRAFT WAKE VORTEX EVOLUTION AND DECAY IN IDEALIZED AND REAL ENVIRONMENTS: METHODOLOGIES, BENEFITS AND LIMITATIONS

F. HOLZÄPFEL, T. HOFBAUER, T. GERZ AND U. SCHUMANN
Institut für Physik der Atmosphäre, DLR Oberpfaffenhofen
D 82234 Weßling, Germany

Abstract.
After a brief introduction of the governing equations and numerical approaches that are used to simulate wake vortices in the atmosphere associated implications and restrictions are discussed. The complex interaction of turbulence and rotation in the vortex core region is not resolved appropriately and is controlled by the subgrid scale model. A local Richardson number correction for strong streamline curvature effects is proposed that accounts for stabilizing effects of coherent rotation and reduces vortex core growth rates. Real case simulations demonstrate that LES is capable to reproduce complex wake vortex behaviour as the spectacular rebound observed at London Heathrow Int'l Airport. Various idealized cases with stably stratified, turbulent and sheared environments are used to reveal the mechanisms that control vortex decay.

1. Introduction

As an unavoidable consequence of lift, aircraft generate counter-rotating pairs of trailing vortices which constitute a potential hazard to following aircraft. Therefore, separation distances between consecutive aircraft were established already in the early 1970s. The incentive of today's wake vortex research is mainly induced by the continuous growth of air traffic which increasingly congests airports during approach and landing. Since meteorological conditions have significant impact on wake vortex evolution, one strategy to achieve a relaxation of the separation distances is to predict weather and vortex behaviour along the glide path. Another approach, especially appealing for the design of new large civil aircraft, is to develop constructive measures that could alleviate wake vortex intensity or selectively accelerate vortex decay.

Since the experimental access to decaying trailing vortices under realistic and well-defined weather conditions is extremely difficult in the required temporal and spatial resolution, investigations which allow for detailed physical interpretations are almost only possible with high-resolution numerical simulations. Large-eddy simulations (LES) constitute *the* tool to analyse wake vortex physics throughout their complete lifespan.

A major restriction of the LES, however, is posed by limitations of the resolution. An adequate resolution of both the turbulent flow in the vortex cores and the length scales of the ambient flow exceeds present computer capabilities by far. Therefore, the impact of the subgrid-scale (SGS) closure on the under-resolved flow regions is analysed in section 3 after a brief introduction of the applied LES method in section 2. We propose a new SGS closure modification for strong streamline curvature effects and discuss its potential in comparison with corrections from literature in section 4. Then, in section 5 the numerical strategies that are applied to simulate a real case with rebounding wake vortices in a turbulent shear flow above complex terrain are presented. Finally, section 6 shows that coherent turbulent structures which are well resolved by LES play the crucial role in the sequence of relevant decay mechanisms under different ambient conditions (turbulence, stable temperature stratification and shear).

2. Numerical Model and Initial Conditions

We apply the two DLR codes MESOSCOP and LESTUF which originally have been developed for studies in atmospheric boundary layers and of stratified, sheared, and homogeneous turbulence, respectively (Schumann *et al.*, 1987; Kaltenbach *et al.*, 1994). In the meantime, various investigations of wake vortex behaviour (e.g. Holzäpfel *et al.*, 2000; Gerz and Ehret, 1997) have been performed with these codes. In space with coordinates $x_i = (x, y, z)$ and time t, both codes solve the mass conservation equation

$$\frac{\partial u_i}{\partial x_i} = 0, \tag{1}$$

and the Navier-Stokes equations for the resolved velocity vector (u, v, w)

$$\frac{\partial u_i}{\partial t} + \frac{\partial}{\partial x_j} u_i u_j = -\frac{1}{\rho} \frac{\partial p}{\partial x_i} - \frac{\partial \tau_{ij}}{\partial x_j} + \beta g \theta \delta_{i3} \tag{2}$$

in an unstationary, incompressible, and three-dimensional fluid flow, where p denotes the dynamic pressure fluctuation. For simulations of thermally stratified flows we employ the Boussinesq-approximated equations and include the buoyancy term $\beta g \theta \delta_{i3}$, where β, g, θ, δ_{ij} are the volumetric expansion coefficient, the magnitude of the gravitational acceleration, potential

temperature and the Kronecker symbol, respectively. Then, also the equation for the resolved potential temperature θ

$$\frac{\partial \theta}{\partial t} + \frac{\partial}{\partial x_j}(u_j\,\theta) + \frac{d\Theta}{dz}u_3 = -\frac{\partial \tau_{\theta j}}{\partial x_j} \tag{3}$$

has to be solved which is written as the deviation from the mean background state Θ. The vertical gradient of the mean temperature of the atmospheric background, $d\Theta/dz$, is set constant in space and time. In equations (2) and (3) friction and heat diffusion are represented by the SGS fluxes of moment, τ_{ij}, and heat, $\tau_{\theta j}$, which result from the non-linear terms in (2) and (3) after filtering on mesh scale. They are parameterized following an ansatz by Deardorff (1970)

$$\tau_{ij} := \overline{u_i''u_j''} - \frac{1}{3}\overline{u_i''u_i''}\delta_{ij} = -2\nu_{sgs}S_{ij}\,; \qquad \tau_{\theta j} = \overline{u_j''\theta''} = -\frac{\nu_{sgs}}{Pr_{sgs}}\frac{\partial \theta}{x_j} \tag{4}$$

with the strain rate tensor

$$S_{ij} = \frac{1}{2}\left(\frac{\partial u_i}{\partial x_j} + \frac{\partial u_j}{\partial x_i}\right)\,. \tag{5}$$

The SGS viscosity ν_{sgs} is modelled by Smagorinsky's approach

$$\nu_{sgs} = (c_S\Delta)^2(2S_{ij}S_{ji})^{1/2}\,, \tag{6}$$

and the constants $c_S = 0.165$ and $Pr_{sgs} = 0.419$ are set to the theoretical values for isotropic turbulence.

Alternatively, an algebraically approximated second order closure method that solves a transport equation for the SGS kinetic energy, $\overline{E''} = \overline{u_i''^2}/2$, and algebraic equations for the anisotropic part of the subgrid scale fluxes

$$\overline{A_{ij}''} = \overline{u_i''u_j''} - \frac{2}{3}\delta_{ij}\overline{E''} \tag{7}$$

is applied in section 5 (for details regarding closure assumptions we refer to Schmidt and Schumann, 1989).

The physical fields are discretized on a Cartesian staggered grid and integrated in space and time by second-order finite differencing. Time advancement is performed by a prognostic step for advection and diffusion using the second-order Adams-Bashforth scheme followed by a diagnostic step which solves the Poisson equation for the dynamic pressure. The integration scheme is non-dissipative and only weakly diffusive.

The computational grid is equidistant in spanwise direction, y, and vertical direction, z, with a typical resolution of $\Delta y = \Delta z = 1\,m$ whereas a

coarser resolution of $\Delta x = 6.4\,m$ is chosen in flight direction, $-x$. When calculating the effective mesh size, Δ, a fitting formula (Scotti *et al.*, 1993) is used to account for the anisotropy of the numerical mesh. A typical domain size corresponds to $L_x \times L_y \times L_z = 408 \times 256 \times 540\,m^3$. In the idealized cases (LESTUF) periodic boundary conditions are employed in all three directions whereas in the real cases (MESOSCOP) no-slip and free-slip conditions are prescribed at the ground and top boundary, respectively. The wake vortex induced initial flowfield displays a small velocity kink across the periodic boundaries. The resulting disturbances are negligible since the boundaries are sufficiently far apart from the primary vortices.

The wake vortices are initialized as superposition of two Lamb-Oseen vortices where the tangential velocity profile of one vortex is given by

$$ v_\theta(r) = \frac{\Gamma_0}{2\pi r}\left(1 - exp\frac{-1.257r^2}{r_c^2}\right). \tag{8} $$

In most simulations a core radius of $r_c = 4\,m$, a root-circulation of $\Gamma_0 = 565\,m^2/s$ and a vortex spacing of $b_0 = 47\,m$ are employed to represent the B-747 aircraft. The type of turbulence initialization in the wake vortices and their environment is different from case to case and will be introduced together with the specific cases.

3. Resolution Requirements and Vortex Core Evolution

The resolution issue is well illustrated with the simulation of wake vortices in a convectively driven atmospheric boundary layer (CBL). Ideally, the resolved length scales should span a range from the order of approximately $0.1\,m$ in the vortex cores to the order of $1000\,m$ in the atmosphere, where the latter length scale roughly corresponds to the inversion height of a CBL. An appropriate equidistant numerical mesh would need $\mathcal{O}(10^{12})$ mesh points, whereas our current grids are limited to about 10^7 meshes.

Appropriate compromises have to be found to conduct such simulations nevertheless. Here, the simulation of wake vortices with unrealistically large initial vortex cores of $r_c = 8\,m$ resolved by four grid points in an *evolving* CBL with an inversion height of $z_i = 512\,m$ enabled to cover the main features of wake vortex interaction with turbulent updrafts and downdrafts in a CBL (Holzäpfel *et al.*, 2000). The CBL simulation was driven by a constant vertical heat flux at the lower surface and three wake vortex pairs were superimposed on the turbulent flowfield after the evolving CBL was well established. Figure 1 illustrates the interaction of convective cells and 10 seconds old wake vortices in a perspective view of an iso-surface of the upwards directed velocity $w = 2\,m/s$.
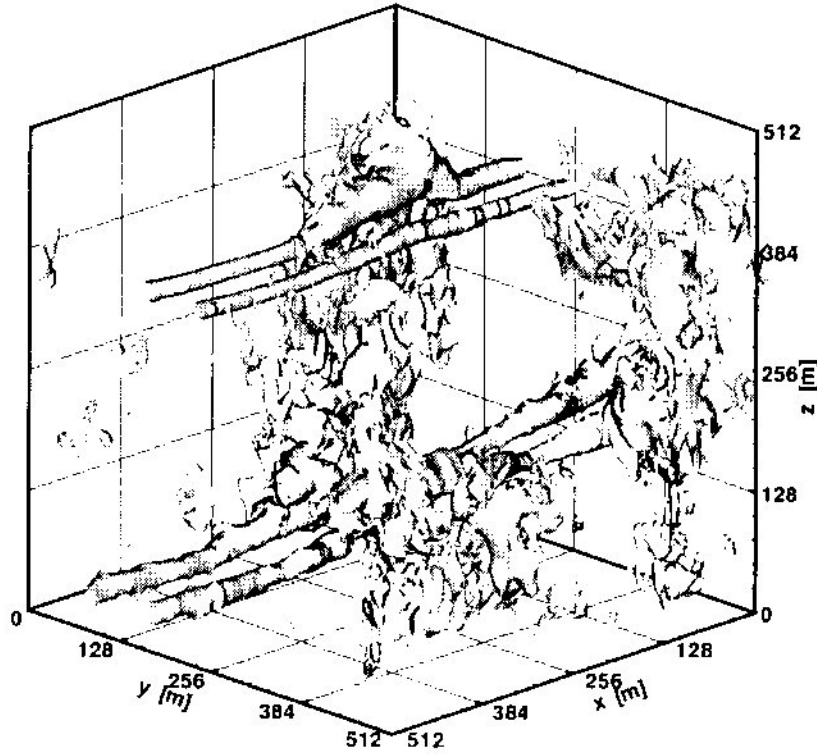
Figure 1. Iso-surface $w = 2\,m/s$ of the evolving CBL with 10 seconds old wake vortices.

Obviously, any LES of wake vortices in the atmosphere will under-resolve the vortex core region. To illustrate the consequential effects, the Smagorinsky eddy viscosity ν_{sgs} (eq. 6) normalized by Γ_0

$$\frac{\nu_{sgs}(r)}{\Gamma_0} = \frac{(c_S \Delta)^2}{\sqrt{2\pi}\, r_c^2} \left(\frac{r_c^2}{r^2} - \left(1.257 + \frac{r_c^2}{r^2} \right) \exp\frac{-1.257 r^2}{r_c^2} \right) \tag{9}$$

is derived for the Lamb-Oseen vortex (eq. 8) and plotted in figure 2 for different models and vortex core resolutions. The strain rate in equation (6) is applied for convenience in curvilinear coordinates, because then solely the radial-tangential component of the strain rate tensor, $r\frac{\partial v_\theta/r}{\partial r}$, contributes to ν_{sgs}. Note that in equation (9) the resolution of the vortex cores, (Δ/r_c), enters to the power of two. Therefore, in poorly resolved vortex cores enhanced values of SGS viscosity are generated (see figure 2) that cause large vortex core growth rates and a strong reduction of peak vorticity. Figure 2 delineates that ν_{sgs} increases from zero[1] at $r = 0$ (rigid body rotation) to a maximum at $1.2\,r_c$ and then decreases again. As a consequence, the radial velocity profiles deviate from the family of self-similar Lamb-Oseen vortex profiles that are achieved in DNS with constant viscosity[2]. For example, a slight overshoot of circulation on $r > 2r_{c0}$ is produced (see figure 3a).

[1]Obviously, when approaching $r = 0$ molecular diffusion becomes relevant. Since this is a singular situation molecular diffusion can be neglected in the LES.

[2]The DNS used in section 5 reached $\nu/\Gamma_0 = 1/Re = 1/5000$. This indicates that only slightly higher vortex Reynolds numbers are achievable by LES with standard Smagorinsky closure compared to DNS.
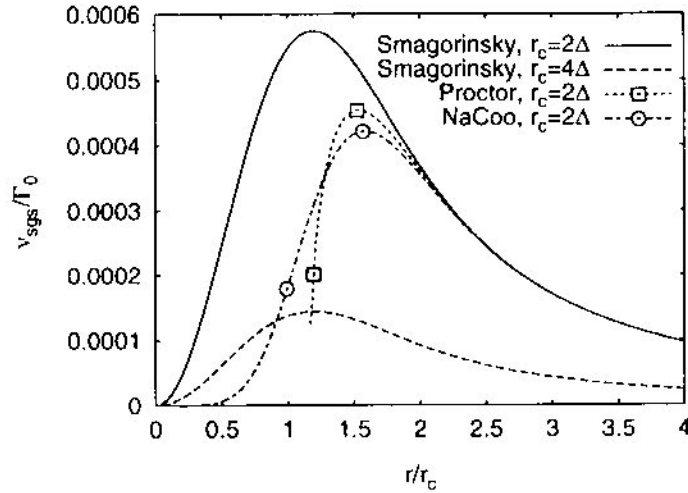
Figure 2.   Radial profiles of normalized eddy viscosity for Smagorinsky closure and modifications with $\alpha = 1$. Modifications are displayed for coarser resolution, $r_c = 2\Delta$, for better readability.

As long as ν_{sgs} is determined by mean velocity gradients (due to limited resolution) and not by gradients of velocity fluctuations, the SGS momentum fluxes should be corrected for streamline curvature effects.

4. SGS model correction for streamline curvature effects

The following considerations are based on the "Richardson number" for streamline curvature effects that Bradshaw (1969) derived in analogy to the gradient Richardson number for buoyancy effects in stably stratified flows. Bradshaw's Richardson number

$$Ri = \frac{2u}{r^2} \frac{\partial ur}{\partial r} \Big/ \left(\frac{\partial u}{\partial r}\right)^2 \tag{10}$$

relates the oscillation frequency squared of a radially displaced fluid element which retains its angular momentum in a flow with curvature of radius r to the square of a "typical frequency scale of the shear flow". However, equation (10) is misleading because it relates the oscillation frequency in natural coordinates to the frequency scale of plane shear taken in an inertial reference frame. As a consequence, in a vortex the Richardson number would go to infinity at $r = r_c$ where erroneously maximum stability would be assumed as done by Cotel and Breidenthal (1999). A consistent formulation is achieved when instead in the denominator the strain rate is employed and both numerator and denominator are expressed in inertial coordinates or, for convenience, in curvilinear coordinates

$$Ri = \frac{2v_\theta}{r^2} \frac{\partial v_\theta r}{\partial r} \Big/ \left(r \frac{\partial v_\theta/r}{\partial r}\right)^2 . \tag{11}$$

For a Lamb-Oseen vortex the Richardson number (11) increases monotonically from zero at $r/r_c > 2$, reaches a value of 2 at $r = r_c$ and goes to infinity when approaching $r = 0$. Proctor extended the Richardson number formulation to three dimensions (see Shen et al., 1999)

$$Ri = \frac{\Omega^2}{D^2} + \frac{\Omega}{D},$$ (12)

where Ω and D are the magnitude of three-dimensional vorticity and deformation tensor, respectively. Since equation (12) cannot discriminate between vorticity of a plane shear flow and vorticity of coherent rotation an additional discriminator algorithm has to be applied. Proctor implements the Richardson number by modifying the SGS viscosity according to

$$\nu_{sgs} = \nu_{sgs,stand}(1 - \alpha Ri)^{0.5},$$ (13)

where α is a constant. We apply instead the corrected ansatz by Bradshaw (11) in natural coordinates (termed NaCoo)

$$Ri = \frac{2v_t}{r}\left(\frac{v_t}{r} + \frac{\partial v_t}{\partial r}\right) \Big/ D^2$$ (14)

that does not require a discriminator function. It employs directly the tangential velocity, v_t, along a local streamline whose curvature is given by an inscribed circle with radius r. The curvature radius is calculated following the approach of Hirsch (1995). In equation (14) the shear vorticity, $\frac{\partial v_t}{\partial r}$, and curvature vorticity, $\frac{v_t}{r}$, just balance each other in the potential vortex. The correction is implemented according to

$$\nu_{sgs} = \nu_{sgs,stand}\frac{1}{1 + \alpha Ri}.$$ (15)

For an undisturbed Lamb-Oseen vortex both Richardson number formulations given in equations (12), (14) yield identical results. The different ν_{sgs}-profiles in figure 2 solely origin from the different implementations (equations (13) and (15)). With both implementations the corrections effectively reduce ν_{sgs} in the vortex core region. With NaCoo ν_{sgs} smoothly goes to small values when approaching the vortex center whereas Proctor's implementation gives a relatively abrupt transition to zero at $r/r_c \approx 1.2$. We prefer the smooth transition for the sake of physical plausibility (maximum stability is reached in the vortex center) and numerical stability.

We performed LES of the evolution of a single Lamb-Oseen vortex with $\Gamma_0 = 565\,m^2/s$ and $r_{c0} = 4\,m$ resolved by four grid points. Figure 3a shows radial profiles of tangential velocity at $t = 0\,s$ and $t = 20\,s$. The comparison of the velocity profiles for the Smagorinsky closure and the
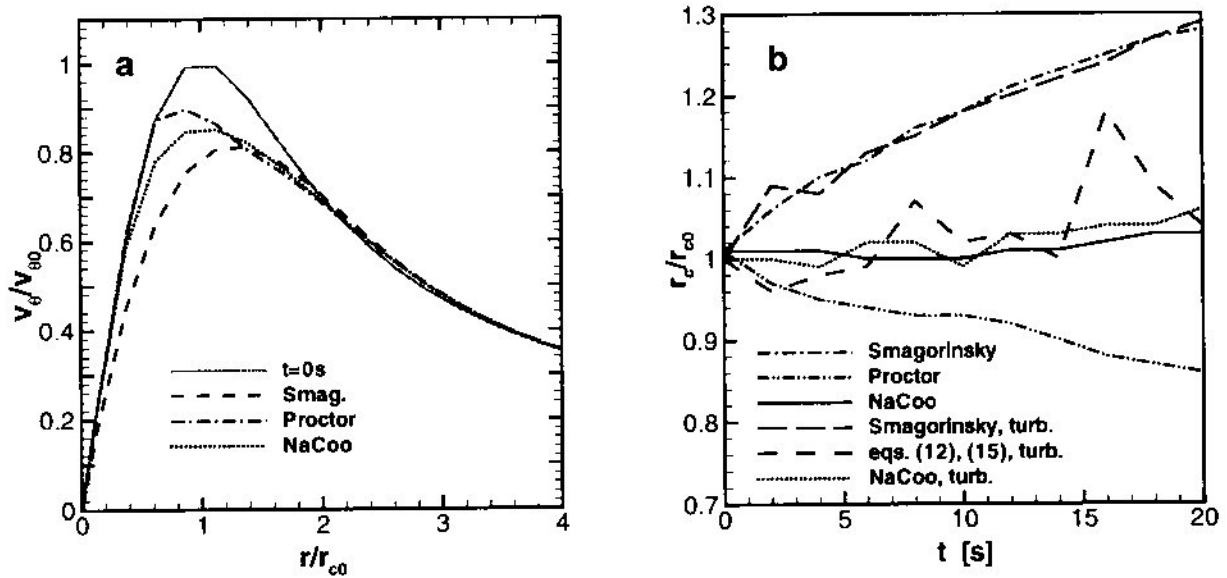
Figure 3. Comparison of Smagorinsky closure and modifications; $\alpha = 1$. a) Radial profiles of tangential velocity at $t = 0\,s$ and $t = 20\,s$. b) Temporal evolution of core radii in laminar and turbulent simulations.

modifications indicates that with the modifications (i) the peak vorticity is well conserved, (ii) the growth of the core radii is retarded, (iii) an outer vortex core between solid body and potential vortex is formed as seen in experimental studies (Jacquin *et al.*, 2001). Furthermore, (iv) the strongly damped diffusivity in the vortex cores allows for vortex core meandering as often observed in experiments (Holzäpfel *et al.*, 1999; Rokhsaz *et al.*, 2000; Jacquin *et al.*, 2001).

Figure 3b delineates the temporal evolution of vortex core radii with and without initially superimposed white noise. In the laminar vortex Proctor's correction even causes shrinking core radii because the region of the velocity maximum experiences diffusion only from larger radii (see figure 2). The large growth rates achieved with standard Smagorinsky are not affected by turbulence. A disadvantage of a vorticity-based Richardson number formulation (12) becomes visible in the turbulent case: Turbulent vorticity patches receive no damping even outside the stable core region which is reflected in the unsteady evolution of core radii. NaCoo, that produces small core growth rates, is not affected by the spotty structure of vorticity because it is controlled by the only marginally distorted streamline curvature (see figure 10). As recent PIV[3] measurements (Vollmers, 2001) proved, the combination of small scale turbulence with coherent rotation, e.g. turbulent vortex cores, typically may occur in wake vortices.
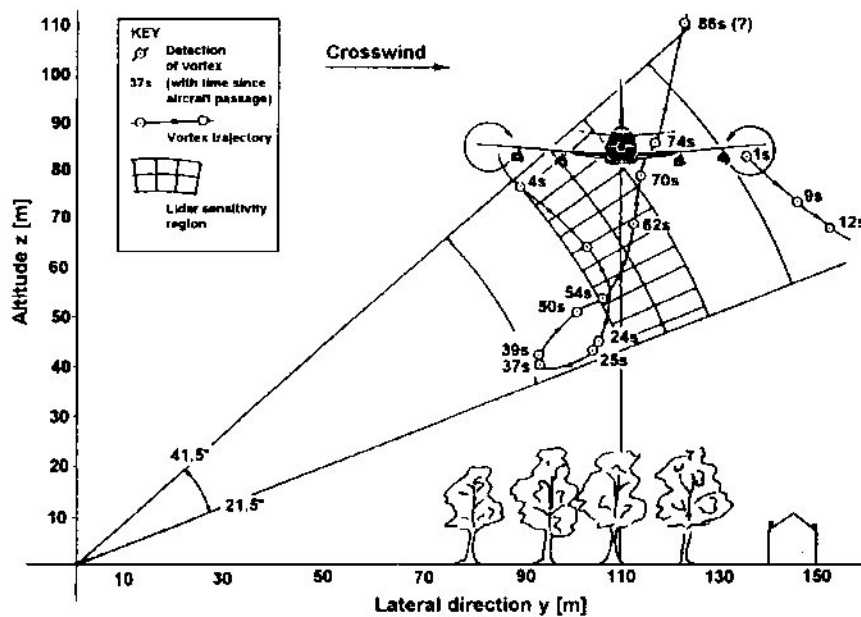
---

[3] *Particle Image Velocimetry*

Figure 4. Reconstruction of vortex trajectories from measured LDV data of a Boeing B747-200 in terminal approach (from Greenwood and Vaughan, 1997)

5. Real Case Simulations

For flight safety reasons, situations of persistent vortices which remain in the flight corridor are of special interest. From LDV[4] field measurements conducted at London-Heathrow Int'l Airport, Greenwood and Vaughan (1997) report such a case. As depicted in figure 4, the upwind vortex of a Boeing B747-200 in terminal approach was found to rebound back to flight level after an initial descent. 70 seconds after the aircraft passage, this vortex again attains generation altitude with practically undiminished strength. Apparently, this situation might have been critical to a follower aircraft, considering typical temporal aircraft spacings of 90 120 seconds. Greenwood and Vaughan suppose that the trees which are also depicted in figure 4 may well have been important in creating the updraft to carry the vortex. Other reasons might have been stable stratification, gusts or a low-altitude jet layer which could have been intensified by the presence of the trees.

In order to find out the possible reasons that might be responsible for the observed vortex behaviour, LES and DNS are conducted. Owing to the complexity of this problem, the simulations have to capture the details of this case, namely the vegetation, the instationarity of the wind, and ambient turbulence.

The initial conditions with respect to appropriate and fully developed

---

[4]*Laser Doppler Velocimetry* Technique to determine the line-of-sight velocity component by measuring the Doppler shift of a Laser beam.
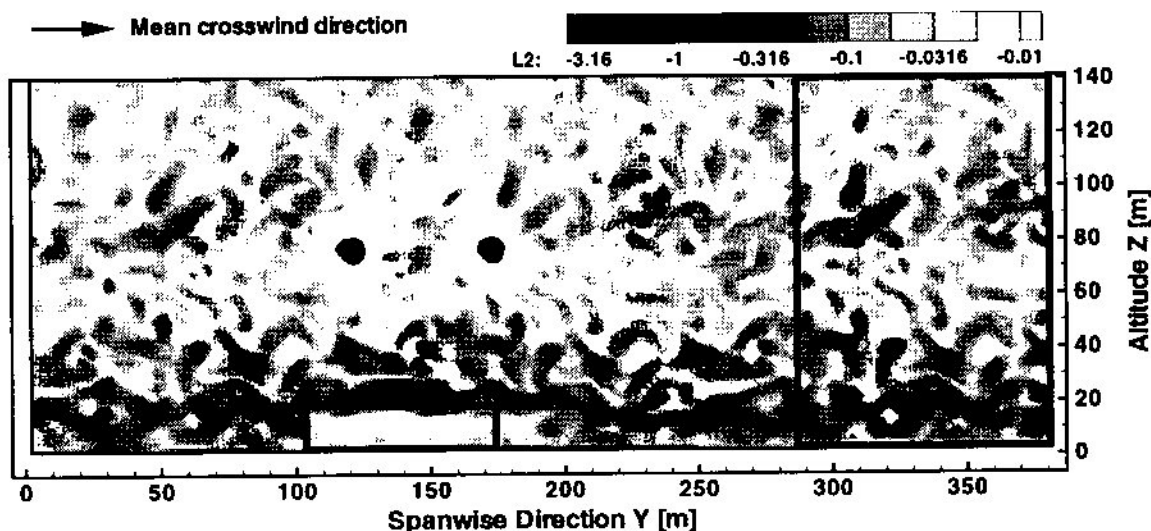
Figure 5. Contour plot of λ_2-contours displaying wake vortices and ambient turbulence in a vertical-lateral cross-section at $t = t_0$. Rectangles indicate area with tree modeling and a relaxation domain.

turbulence are obtained by a preparatory run which in turn starts by superimposing the mean wind with homogeneous isotropic turbulence. Once the turbulence has adapted to the inhomogeneity of the environmental conditions, e.g. the ground, and a quasi steady-state is reached, the wake vortices are injected at $t = t_0$. Figure 5 displays the turbulence field right after vortex injection in a vertical-lateral cross-section of λ_2-contours[5]. The corresponding domain size is $L_x \times L_y \times L_z = 48 \times 384 \times 144\,m^3$ with a resolution of $\Delta x \times \Delta y \times \Delta z = 3 \times 1 \times 1 \times m^3$.

During the field measurement, a second LDV – approximately $30\,m$ upstream of the first one – was used to measure the ambient wind velocity. In order to account for the unsteadiness of the measured wind, a relaxation scheme is employed in the downstream region of the simulation domain. In the relaxation domain the mean velocities are forced to gradually adapt to the measured velocities. Figure 6a shows good agreement between measured and modeled vertical crosswind profiles prior to vortex injection.

The trees that are suspected to influence the vortex trajectories are modeled according to Shaw and Schumann (1992) by embedding a momentum sink, $-c_d a |\vec{V}| u_i$, in equation (2). The drag coefficient, c_d, is set to 0.15 and the leaf area density, a, is prescribed as displayed in figure 6b.

The comparison of measured and LES vortex trajectories in figure 7a shows excellent agreement. Alternatively employed DNS yield almost identical trajectories which indicates that at least vortex trajectories are insensitive to vortex core evolution. Neglecting the axial wind component (figure 7b) also leads to very similar results. However, without the group of trees no rebound is observed. We argue that the combined effects of the trees

---

[5] λ_2 is a measure for coherent vortex structures according to Jeong and Hussain (1995).
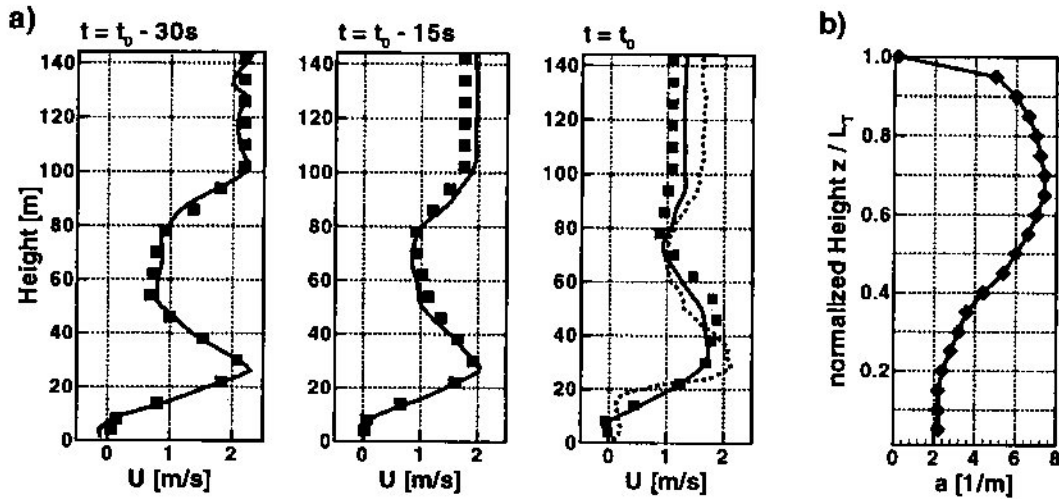
Figure 6. a) Measured (symbols) and forced (lines) axially averaged crosswind profiles at $y = 0$ and different instants in time. Dotted curve denotes wind profile at $y = 140\,m$. b) Vertical profile of leaf area density.
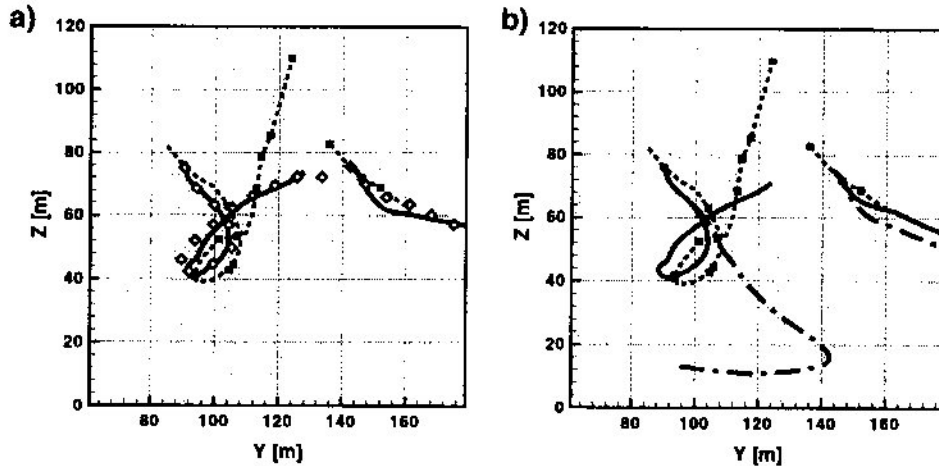

Figure 7. Measured (full squares) and simulated vortex trajectories a) with fully detailed simulation set-up for LES (full line) and, alternatively, DNS (diamonds); b) neglecting axial wind component (full line) or neglecting tree modeling (dash-dotted), respectively.

acting as elevated ground and the positive crosswind shear that is produced above the trees (see figure 6a) are mainly responsable for the remarkable rebound. On the other hand, the simulations show that some high level of detail is necessary to reproduce such striking real case vortex behaviour.

6. Decay Mechanisms

Although the streamline curvature correction (section 4) allows for more realistic modeling of vortex core evolution, only minor deviations in overall wake vortex behaviour are found in simulations of wake vortices in a quiescent or a turbulent atmosphere. Therefore, we conclude that an inadequate resolution of vortex cores constitutes a minor restriction of universality and that, as we will show below, well-resolved coherent secondary vorticity structures determine the decay.

Although these vorticity structures originate from different sources in the investigated cases (i) a stably stratified, quiescent atmosphere, (ii) a turbulent atmosphere, (iii) a stably stratified, turbulent atmosphere, and (iv) a turbulent low-level jet (see Holzäpfel et al. (2001) for cases (i)–(iii), Hofbauer and Gerz (2000) for case (iv)) - the underlying mechanisms that trigger decay are very similar.

Different phases that control vortex decay are identified: (1) the specific environmental conditions (i)-(iv) introduce secondary vorticity in the vicinity of the wake vortices, (2) this vorticity is intensified by vortex stretching in the wake vortex induced velocity field, (3) the produced coherent vortical structures wrap around the primary vortices, and (4) – again by velocity induction – deform the vortex cores, destabilize the vortices and enable vorticity exchange between the vortex pair and its surroundings. Finally, (5) these mechanisms lead to a phase of rapid decay. The interrelation of azimuthal vorticity structures and wake vortex decay was first pointed out by Risso et al. (1994) and is typical for three-dimensional turbulence initialization (Kleiser and Schumann, 1984).

In cases (ii), (iii) moderate, anisotropic, and decaying atmospheric turbulence is superimposed on the whole velocity field. The atmospheric turbulence, which is described in detail in Gerz and Holzäpfel (1999), obeys prescribed spectra with rms velocities of $0.38 \, m/s$ in horizontal and $0.21 \, m/s$ in vertical direction. The length scales of the most energetic eddies amount to 60 to 90 m. Turbulence induced by the aircraft was taken into account in cases (i)–(iii) by adding initially a three-dimensional random perturbation field to the swirling flow such that the perturbations reach maximum rms values of $2 \, m/s$ at the core radius, r_c, and decay exponentially for smaller and larger radii. In the stably stratified case (iii) the prescribed constant potential temperature gradient of the atmosphere was $d\Theta/dz = 5 \, K/100 \, m$.

Figure 8 depicts iso-contours of the lateral and vertical vorticity components that are induced by the wake vortices in a turbulent atmosphere.[6] Wake vortices are represented by tubular λ_2-contours. The iso-lines of the lateral velocity, v, illustrate the converging flow that is induced by the wake

---

[6]For coloured figures see http://www.pa.op.dlr.de/wirbelschleppe/EUROM.html
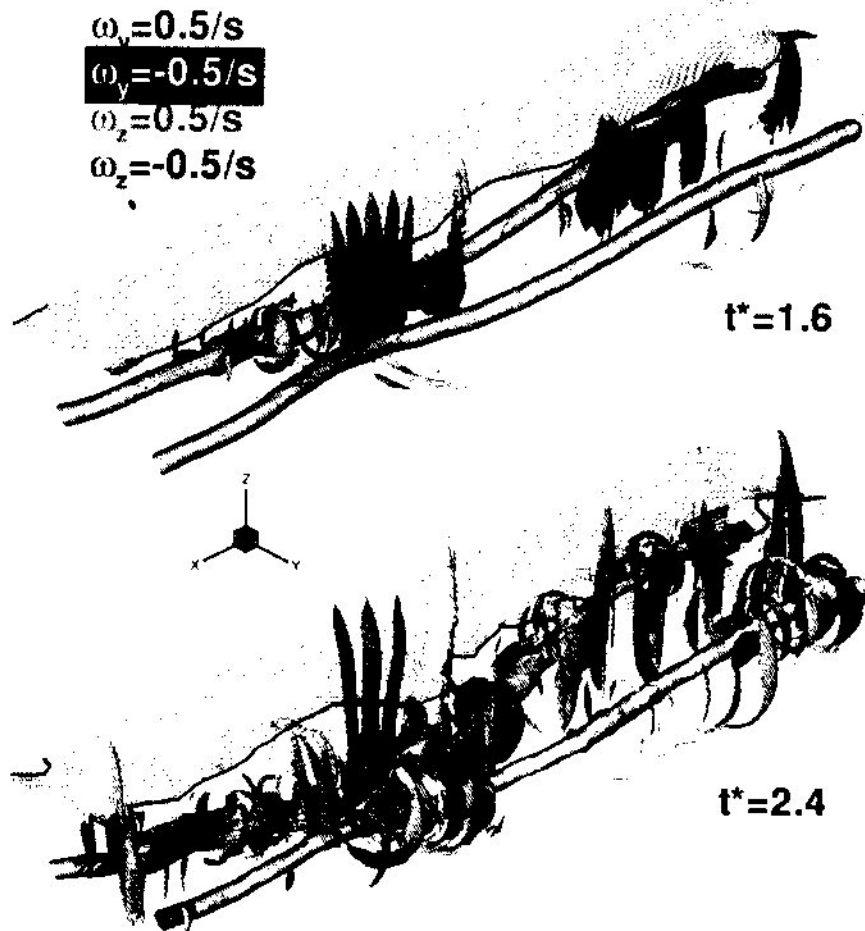
Figure 8. Decay in turbulent atmosphere; case (ii). Iso surfaces of lateral and vertical vorticity components in a perspective view and iso-lines for lateral velocity, v, in a horizontal plane above the vortices. Wake vortices are represented by tubular λ_2-contours. Dimensionless time $t^* = t/t'$ is normalized by the time scale $t' = 2\pi b_0^2/\Gamma_0$.

vortices above. This converging flow is deformed by superimposed atmospheric turbulence such that the iso-line $v = 0$ (bold) meanders along the symmetry plane between the vortices. As described in quantitative detail for case (i) in Holzäpfel *et al.* (2001), this superposition of turbulent and wake vortex induced velocities produces axial gradients of the lateral velocity, $\partial v/\partial x$, and, equivalently, vertical vorticity, $\omega_z \sim \partial v/\partial x$ in a volume above and midway between the vortices. The resulting vertical vorticity streaks, ω_z, (see figure 8) are amplified by vortex stretching due to the acceleration of the downwards directed flow between the main vortices. Then, the vorticity is tilted, and wraps around the primary vortices.

In the stably stratified case (iii) (figure 9) these effects are even more pronounced and develop faster. Here, it is the baroclinic vorticity, ω_x, that additionally induces lateral velocities above the vortices that are directed towards the symmetry plane and intensifies the axial gradients of the lateral velocity. (Baroclinic vorticity is produced along the oval-shaped interface
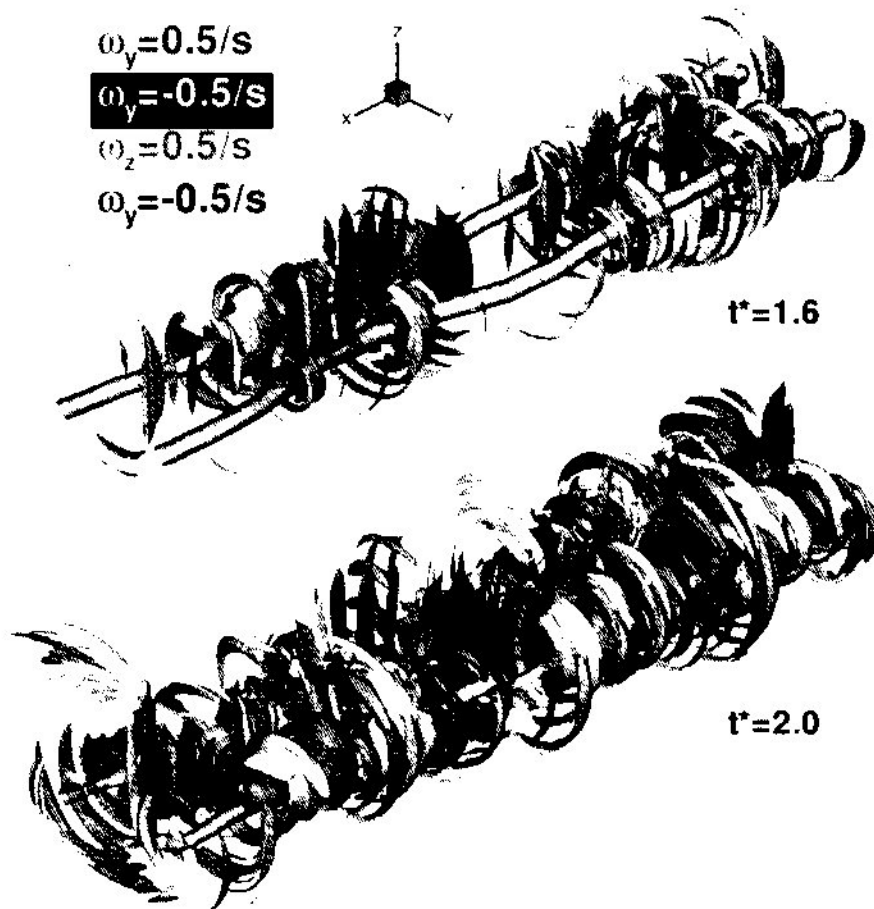
$\omega_y=0.5/s$
$\omega_y=-0.5/s$
$\omega_z=0.5/s$
$\omega_y=-0.5/s$

$t^*=1.6$

$t^*=2.0$

Figure 9. Decay in turbulent stably stratified atmosphere; case (iii). Perspective view of lateral and vertical vorticity components and λ_2-contours.

between the ambient flow and the adiabatically heated flow that descends with the vortices (Holzäpfel and Gerz, 1999)). Note that the induced vorticity structures in case (iii) at $t^* = 2$ are much more intense than in case (ii) at $t^* = 2.4$. They initiate a phase of rapid circulation decay (Proctor and Switzer, 2000; Holzäpfel *et al.*, 2001). The transition to rapid decay coincides with a transition to fully turbulent vortices as illustrated exemplarily in figure 10 for the evolution of wake vortices in a quiescent atmosphere.

Similar mechanisms also control the decay of a trailing vortex pair that immerges into a turbulent low-level jet as seen in figure 11 (for details see Hofbauer and Gerz, 2000). In a preparatory run that was performed in a smaller domain the jet was allowed to develop from an initial isotropic state with root-mean-square velocity fluctuations of 5% of the maximum jet velocity. For the main simulation the jet was composed of two identical streamwise segments and the wake vortices were injected above the jet. The visual comparison of the formerly identical vorticity structures in the two parts of the jet allows to identify the interaction of jet turbulence and wake vortex induced velocity field. Clearly visible the jet vorticity is inten-
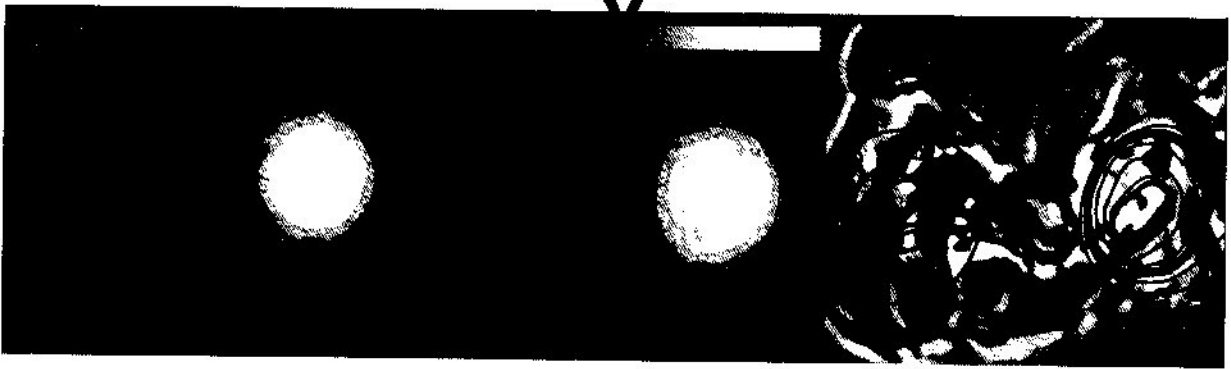
Figure 10. Vertical-lateral cross-sections of axial vorticity. Simulation of wake vortices initialized with aircraft induced-turbulence in a quiescent atmosphere employing the Richardson number correction NaCoo.
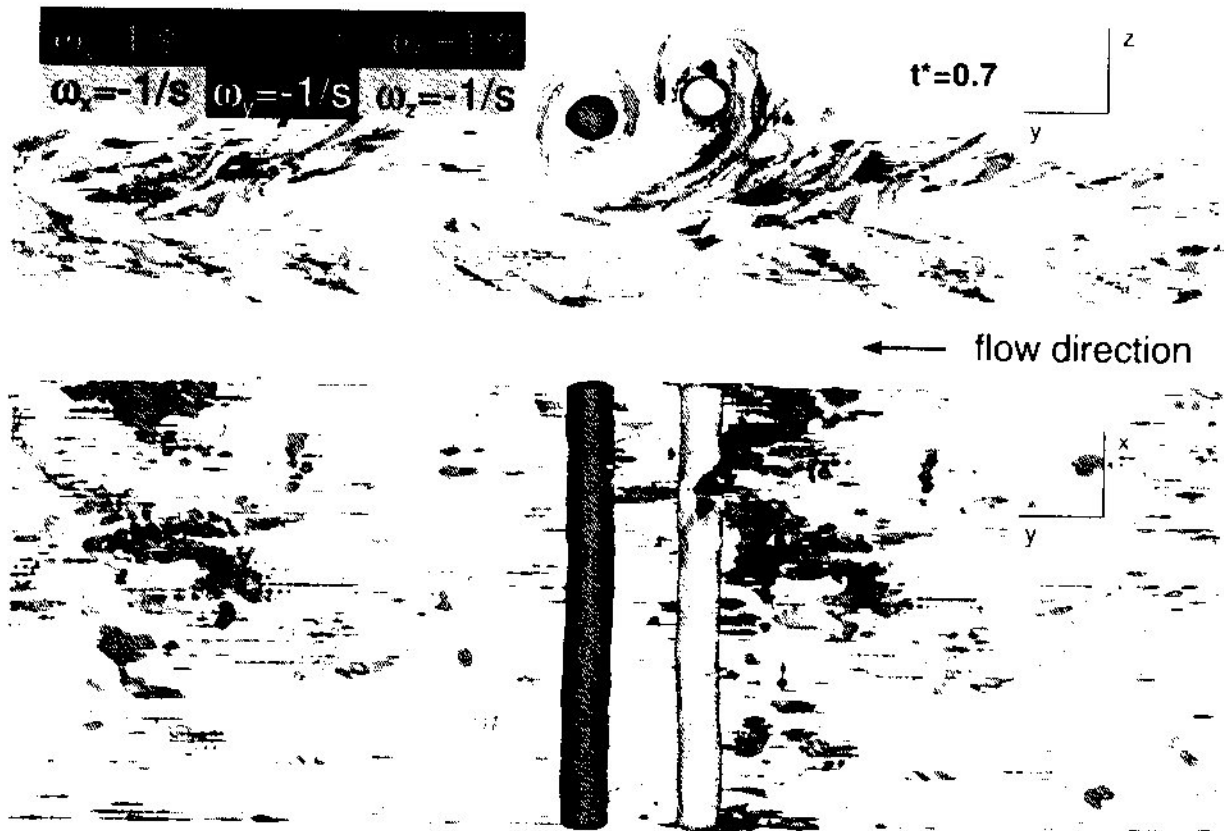

Figure 11. Wake vortices immerging into a turbulent low-level jet. Iso-contours of all three vorticity components in a front view and a top view.

sified along the upstream flank of the deformed wake vortex oval. At this flank a "stagnation line" forms and the jet-induced vorticity structures are stretched when torn apart in the wake vortex induced velocity field. Figure 12 shows in a perspective view how the intensified vorticity structures enclose the upstream vortex like a breaking wave.
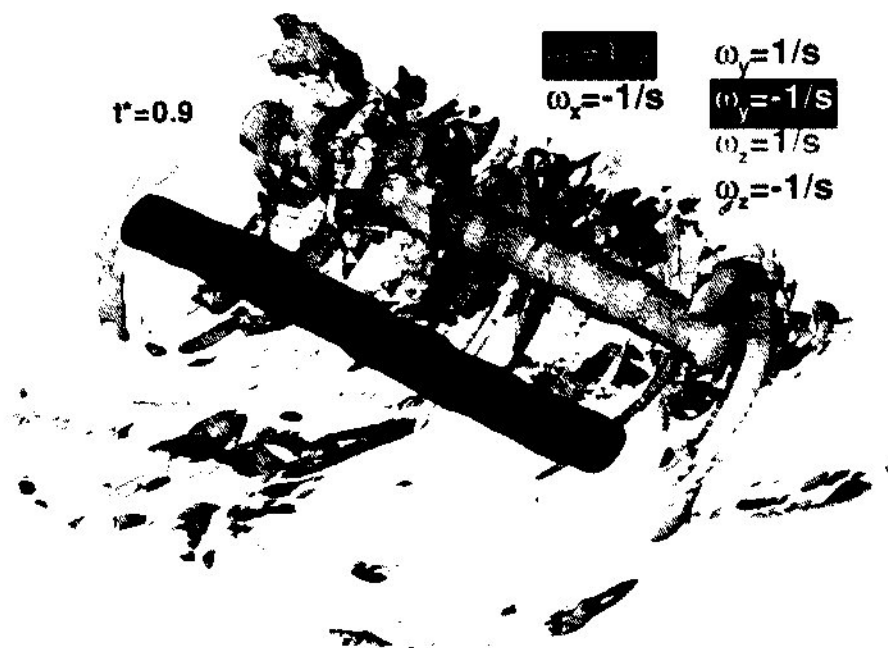
Figure 12. Perspective view of jet vortex interaction. Iso-contours of all three vorticity components.

7. Conclusions

We elucidate the implications and restrictions that are connected to the unavoidably inadequate resolution of wake vortex simulations in the atmosphere. To alleviate these restrictions a Richardson number correction is proposed that accounts for streamline curvature effects in the subgrid scales and reduces unrealistic vortex core growth rates. However, the improved approximation of realistic vortex core evolution does not modify vortex trajectories and decay essentially. In the atmosphere decay is controlled by well-resolved processes of vorticity intensification caused by stretching of environmental vorticity in the wake vortex induced flowfield. The generality of the involved mechanisms is illustrated with examples comprising stably stratified, turbulent and sheared environments. The example of the impressive wake vortex rebound measured at London-Heathrow airport demonstrates the capability of LES to reproduce complex real cases and to reveal the decisive underlying physical mechanisms.

References

Bradshaw, P. (1969) The analogy between streamline curvature and buoyancy in turbulent shear flow, *J. Fluid Mech.* **36**, pp. 177–191

Cotel, A.J. and Breidenthal, R.E. (1999) Turbulence inside a vortex, *Phys. Fluids* **11**, pp. 3026-3029

Deardorff, J.W. (1970) A numerical study of three-dimensional turbulent channel flow at large Reynolds numbers, *J. Fluid Mech.* **41**, pp. 453 480

Gerz, T. and Ehret, T. (1997) Wingtip vortices and exhaust jets during the jet regime of aircraft wakes, *Aerospace Sci. Techn.* **1**, pp. 463-474

Gerz, T. and Holzäpfel, F. (1999), Wingtip vortices, turbulence, and the distribution of emissions, *AIAA J.* **37**, pp. 1270-1276

Greenwood, J.S. and Vaughan, J.M. (1997) Measurements of Aircraft Wake Vortices at Heathrow by Laser Doppler Velocimetry, Air Traffic Control Quarterly **6**, pp. 179-203

Hirsch, C. (1995) Ein Beitrag zur Wechselwirkung von Turbulenz und Drall, Ph.D. Dissertation, Universität Karlsruhe

Hofbauer, T. and Gerz, T. (2000) Shear layer effects on the dynamics of a counter rotating vortex pair, *AIAA Paper 2000-0758*

Holzäpfel, F. and Gerz, T. (1999) Two-Dimensional Wake Vortex Physics in the Stably Stratified Atmosphere, *Aerospace Sci. Techn.* **3**, pp. 261-270

Holzäpfel, F., Gerz, T. and Baumann, R. (2001) The turbulent decay of trailing vortex pairs in stably stratified environments, *Aerospace Sci. Techn.* **5**, pp. 95-108

Holzäpfel, F., Gerz, T., Frech, M. and Dörnbrack, A. (2000) Wake Vortices in a Convective Boundary Layer and Their Influence on Following Aircraft, *J. of Aircraft* **37**, pp. 1001-1007

Holzäpfel, F., Lenze B. and Leuckel W. (1999) Quintuple Hot-Wire Measurements of the Turbulence Structure in Confined Swirling Flows, *J. of Fluids Engineering* **121**, pp. 517-525

Jacquin, L., Fabre, D. and Geffroy, P. (2001) The Properties of a Transport Aircraft Wake in the Extended Near Field: an Experimental Study, *AIAA Paper 2001-1038*

Jeong, J. and Hussain, F. (1995) On the identification of a vortex, *J. Fluid Mech.* **285**, pp. 69-94

Kaltenbach, H.-J., Gerz, T. and Schumann, U. (1994) Large-eddy simulation of homogeneous turbulence and diffusion in stably stratified shear flow, *J. Fluid Mech.* **280**, pp. 1-40

Kleiser L. and Schumann, U. (1984) Spectral simulations of the laminar-turbulent transition process in plane poiseuille flow, *Spectral methods for partial differential equations*, SIAM, Philadelphia, pp. 141-163

Proctor, F.H. and Switzer, G.F. (2000) Numerical Simulation of Aircraft Trailing Vortices, *9th Conf. on Aviation, Range and Aerospace Meteorlogy* **7.12**, pp. 511 516

Risso, F., Corjon, A. and Stoessel, A. (1997) Direct numerical simulations of wake vortices in intense homogeneous turbulence, *AIAA J.* **35**, pp. 1030-1040

Rokhsaz, K., Foster, S.R. and Miller, L.S. (2000) Exploratory Study of Aircraft Wake Vortex Filaments in a Water Tunnel, *J. of Aircraft* **37**, pp. 1022-1027

Schmidt, H. and Schumann, U. (1989) Coherent structure of the convective boundary layer derived from large-eddy simulations, *J. Fluid Mech.* **200**, pp. 511-562

Schumann, U., Hauf, T., Höller, H., Schmidt, H. and Volkert, H. (1987) A mesoscale model for the simulation of turbulence, clouds and flow over mountains: Formulation and validation examples, *Beitr. Phys. Atmosph.* **60**, pp. 413-446

Scotti, A., Meneveau, C. and Lilly, D.K. (1993) Generalized Smagorinsky model for anisotropic grids, *Phys. Fluids* A **5**, pp. 2306-2308

Shaw, R.H. and Schumann, U. (1992) Large-Eddy Simulation of Turbulent Flow above and within a Forrest, *Boundary-Layer Meteorology* **61**, pp. 47 64

Shen, S., Ding, F., Han, J., Lin, Y.-L., Arya S.P. and Proctor, F.H. (1999) Numerical Modeling Studies of Wake Vortices: Real Case Simulations, *AIAA Paper 99-0755*

Vollmers, H. (2001) Detection of vortices and quantitative evaluation of their main parameters from experimental velocity data, submitted to *Meas. Sci. Technol.*